Available online at www.sciencedirect.com
ScienceDirect
International Journal of Thermal Sciences 46 (2007) 1126–1141
International Journal of Thermal Sciences
www.elsevier.com/locate/ijts

Analysis of turbulence in a micro-channel emulsifier ☆

Slawomir Blonski, Piotr M. Korczyk, Tomasz A. Kowalewski *

[a] *Institute of Fundamental Technological Research, Polish Academy of Sciences, Swietokrzyska 21, 00-049 Warsaw, Poland*

Received 8 July 2006; received in revised form 8 December 2006; accepted 28 January 2007

Available online 26 March 2007

Abstract

Turbulent flow of water in an 1 mm long and 0.4 mm high gap of an emulsifier is investigated experimentally using micro-PIV technique and compared with numerical predictions. The purpose of the investigations is to develop a procedure for well-controlled generation of mono-disperse suspension of micro-droplets. The micro-flow measurements are based on epi-fluorescence illumination and high-speed imaging. The experimental data are compared with the numerical results obtained using direct simulation and turbulent flow model. From the turbulent modelling ($k-\varepsilon$) it was found that, the maximum of turbulent energy dissipation rate takes place mainly in the micro-channel gap. However, measured and directly simulated (DNS) velocity fields indicate that flow turbulization is delayed and develops shortly behind the gap. Experimental and numerical results are used to predict droplet dimension of two different oil emulsions. Very low amount of oil-phase fraction in investigated emulsions justifies us to use flow characteristics evaluated for pure water to predict mean diameter of oil droplets. These predictions are validated using experimental data on statistics of droplets size.
© 2007 Elsevier Masson SAS. All rights reserved.

Keywords: Micro-flow; Micro-PIV; Particle Image Velocimetry; Turbulence; Micro-channel; Emulsion

1. Introduction

The design of new procedures for fabrication of nano-structured materials is one of the "hot topics" in the contemporary materials science due to the great potential for their application in various modern technologies. Preparation of micro- and nano-size structures is a fundamental topic of research in this area. The present work was stimulated by request to use droplets of emulsion as a matrix for collecting nano-particles into well structured configuration [1,2]. Production of micro- and nano-size droplets and bubbles gains special interest in several nano-technology applications, like manufacturing of well structured materials, drug delivery in medicine or additives in food industry. Much interest in formation of micro-droplets is motivated by the prospect to conduct chemical reactions in a micro-scale (Lab-on-Chip). Micro-fluidic devices may provide the ability to design system in which every droplet can be individually processed and analysed, enormously increasing number of possible reactions. An excellent review on recent achievements in controlled formation of micro-droplets can be found by Garstecki et al. [3].

Despite immense progress, in most cases micro-fluidic devices are able to deliver only small volume of dispersed media. Massive production of fine emulsion, necessary for example to develop self-assembled nano-structures, can be achieved only by controlled droplet break-up in a shear flow. The experimental and numerical work presented here is focused on production of emulsion droplets in turbulent flow using a narrow-gap homogeniser. Although this method for production of emulsions is commonly used in industrial applications, the main features and the appropriate conditions for emulsification in such systems are virtually unknown and mainly based on empirical relations.

The final drop size distribution, obtained after an emulsification process in turbulent flow, is a result of dynamic equilibrium between drop breakage and drop–drop coalescence. Various factors and effects, such as kinetics of emulsifier adsorption and interactions between the drops, are known to be of importance, but their quantitative analysis is still missing in the literature.

☆ Part of this paper was presented at ASME International Conference on Nano-, Micro- and Mini-Channels, Limmeric, June 2006.

* Corresponding author. Tel.: +48228269803; fax: +48228274699.
E-mail address: tkowale@ippt.gov.pl (T.A. Kowalewski).

1290-0729/$ – see front matter © 2007 Elsevier Masson SAS. All rights reserved.
doi:10.1016/j.ijthermalsci.2007.01.028

Nomenclature

d	Diameter	m	
G	Velocity gradient	s^{-1}	
I	Turbulence intensity		
p	Pressure	Pa	
Re	Reynolds number		
TKE	Turbulent Kinetic Energy	$m^2 s^{-2}$	
tke_{xz}	Modified Turbulent Kinetic Energy	$m^2 s^{-2}$	
$S^{\parallel}$	Longitudinal structure function	$m^2 s^{-2}$	
$S^{\perp}$	Transverse structure function	$m^2 s^{-2}$	
Q_V	Volumetric flow rate	$m^3 s^{-1}$	
Q_M	Mass flow rate	$kg s^{-1}$	
V	Velocity	$m s^{-1}$	
$\langle V \rangle$	Mean value of velocity	$m s^{-1}$	
V'	Fluctuation of velocity	$m s^{-1}$	
ε	Turbulent Dissipation Rate	$m^2 s^{-3}$	
μ	Viscosity	Pa s	
ρ	Density	$kg m^{-3}$	
σ	Interfacial tension	$N m^{-1}$	

A common feature of the emulsification procedures is that they involve an interplay between capillary and hydrodynamic forces, which determine the final outcome of the emulsification process. The type of flow and the mechanism of emulsification depend not only on the used device, but on the properties of the emulsified phases, as well. In practice, mixed regimes are frequently realized, in which both viscous and inertial forces contribute simultaneously to the emulsification. The understanding of this process is possible only by combining several experimental methods and theoretical approaches.

There are various techniques of emulsification. Most of them are based on the turbulent stirring of two liquids. The process is very effective but produces relatively non-homogenous emulsions. The facility considered here enhances droplets breakup by forcing the emulsion through a rapid contraction. In the tube it creates an axially-symmetric emulsifier, device thoroughly investigated experimentally by Tscholakova et al. [1]. The numerical simulation of the flow through the axially-symmetric emulsifier [1,4] was used to analyze effects of the turbulent energy dissipation on the emulsification process. It was correlated with a droplet size measurements. However, due to the optical constrains of the axial-type emulsifier the droplets break-up mechanism and the flow pattern in the emulsifier could not be validated experimentally.

The main aim of the present work is to determine experimentally details of the flow characteristics in a plane model of the emulsifier, which preserves all hydrodynamic characteristics of the axial-type device [4]. An optical access through transparent walls permitted full field measurements necessary to resolve details of spatial and temporal flow field fluctuations in the emulsifier. The experiment allowed for validation of the numerical model and verification of existing theoretical considerations used to model emulsification process.

The paper deals with a flow of very dilute emulsions. In all investigated emulsions volumetric fraction of dispersed phase did not exceed 1%. This limitation is necessary for applying optical methods in evaluating droplets size. Even having that low concentration of droplets, the velocity measurements were possible for a single phase only, i.e. for the flow of the carrier liquid without droplets. Nevertheless, we assume that flow characteristics measured for single phase are representative for the same flow in the presence of very dilute suspension of droplets, i.e. that there is only one-way coupling: from the carrier liquid on the droplets and not from the droplets back to the continuous phase. Such assumption is justified for dilute suspensions both in laminar flow regime [5], and in turbulent flow [6]. However, for turbulent flow one cannot exclude occurrence of clustering and coalescence of droplets caused by the gradient of the fluctuating velocity field [7]. Such effects are not considered in the present study.

The need to get detailed and accurate measurements in micro-scale of the device enforces the application of new experimental techniques, unusual in classical fluid mechanics. One of them is micro-PIV, full field microscopic velocity measurement using fluorescent tracers with dimension of only several nano-meters. The technique refers to the application of PIV to measure velocity fields of fluid motion with length scales of the order of 100 micrometers, and with spatial resolution of individual velocity measurements of the order of 1–10 micrometers. Due to the small dimensions light sheet technique, typical for macro-scale PIV, cannot be applied for flow illumination, and the whole investigated volume is flooded with light. Images of individual tracers, necessary for PIV evaluation, are obtained by taking advantage of fluorescence, removing by appropriate filters diffused light originating from the bulk illumination. The emphasis of contemporary micro-PIV is placed on its ability to accurately and reliably measure two-dimensional velocity fields with spatial resolution even below limits imposed by optical diffraction [8].

Fundamentals of the micro-PIV method were established by Santiago et al. [9], who used a mercury arc lamp to continuously illuminate 300 nm fluorescent tracers. Using a microscope, an image intensified CCD camera and narrow wavelength optical filter they obtained discrete images of the fluorescent tracers. Correlation analysis was then applied to the particle image field, producing regularly spaced velocity field. The flow fields measured under the microscope characterize high relative velocity due to the large spatial magnification of recorded tracer displacements. It limits magnitude of the velocity to about 0.1 mm/s for epi-fluorescent systems equipped with a mercury lamp. Meinhart at al. [10] succeeded to apply a double pulsed Nd:Yag laser for illumination of 200 nm fluorescent beds suspended in the micro-flow. The very short laser pulse duration (5 ns) allowed them to evaluate under a microscope velocity fields of several cm/s with a spatial resolution below 1 μm.

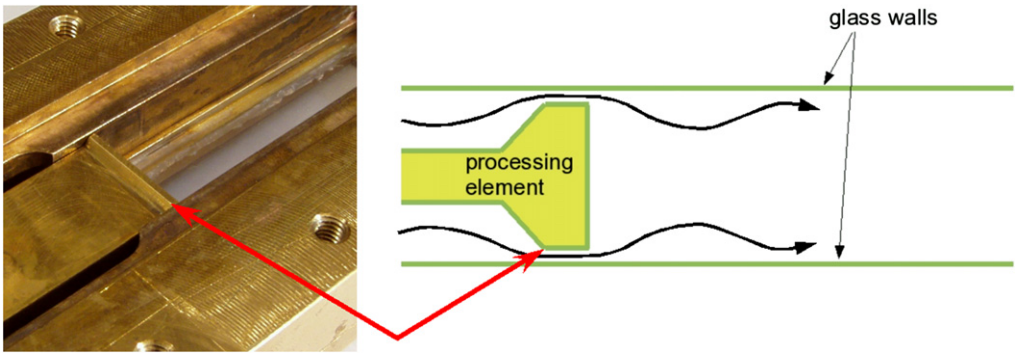

Fig. 1. Model of the narrow-gap homogeniser: top view after removing covering glass wall and schematic cross-section; arrows point to the analysed micro-channel.

The majority of investigations performed in micro-channels are limited to steady, low Reynolds number flows. It is mainly due to the experimental constrains, which demand high speed imaging systems and high pressures to enforce the flow. The present paper reports on micro-PIV measurements performed for flow velocities of several m/s in a channel of 400 μm height. To our knowledge there are very few reports on micro-flow measurements in this range of parameters. Recently Li and Olsen [11] investigated turbulent flow of liquid in a micro-channel. Their excellent experiment declined prior suggestions on the early transition to turbulence in micro-channels. In fact, the main result of our paper claims even possible delayed transition to turbulence. At high Reynolds number ($Re = 8000$) flow measured within a short micro-channel of the investigated emulsifier appears to be quasi-laminar.

2. Experimental setup and procedure

The flow of pure water and of oil/water emulsions was studied for a flat emulsifier assembled at the University of Sophia. The flat emulsifier was constructed to ease optical access, hence to permit application of optical methods for measuring flow velocity fields (PIV method) and to visualize break-up of emulsion droplets. It is a two dimensional substitute of the central cross-section of the axially-symmetric emulsifier thoroughly investigated in the separate study [1,4]. The emulsifier consists of a small channel formed between two glass plates and a triangular processing element creating the rapid flow contraction (Fig. 1). Dimensions of the gap between glass plates and processing element (triangular obstacle) are 0.4 mm in height, 1 mm in length and 15 mm in width (comp. Fig. 2). The processing element forms two inlets of rectangular shape, they are 15 mm wide and 1.5 mm high. After passing the gap flow geometry abruptly changes, filling 15 mm wide and 7.5 mm high outlet. The total length of the inlet segment is equal 97.5 mm and length of the outlet segment is equal 78.5 mm. These physical dimensions were implemented as a computational domain used to simulate flow in the emulsifier (comp. Fig. 12). The inlet and outlet of the channel are connected through 8 mm tubes with the liquid supply system. The flow rate used in the experiments is $Q_V = 0.204\ \mathrm{dm^3\,s^{-1}}$. A typical value of the velocity in the emulsifier is about $5\ \mathrm{m\,s^{-1}}$ for the entrance region and $20\ \mathrm{m\,s^{-1}}$ in the gaps, which corresponds to Reynolds number 7500 and 8000, respectively.

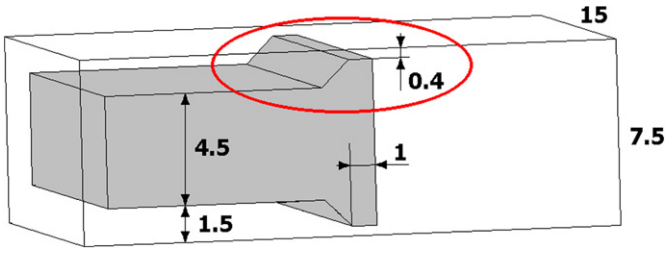

Fig. 2. Geometry of the processing element of the emulsifier model and location of the analysed micro-channel; micro-channel size: height 0.4 mm, width 15 mm and length 1 mm.

The main part of the experimental set-up consists of epi-fluorescence microscope, model of the emulsifier with transparent windows, light source and digital cameras (Fig. 3). A pressurized nitrogen vessel, attached to the working liquid supply bottle was used to pump the liquid through the system. The gas pressure was stabilized at a selected level using the pressure compensation reservoir. Under applied gas pressure the liquid was driven through the homogeniser to the collecting bottle. The flow rate was set varying the reservoir pressure and using the system of valves. The exact value of the flow rate was obtained by measuring the time necessary to fill up a calibrated quantity in the collecting bottle.

Two separate experimental campaigns were performed. In the first experimental campaign velocity fields were measured for pure water flow within the gap and close behind using the micro-PIV system. In the second experimental campaign flow of very dilute water-oil emulsion was investigated. A high speed imaging system was used to collect images of droplets. When the emulsion was used, the experiment was repeated several times by pouring liquid from the collecting bottle back to the supply bottle using a by-pass tube. It was commenced after "manual-shaking" of water–oil mixture prepared in the supply bottle. Usually 5 to 10 passes were used to record the development of the emulsion in the vicinity of the processing element. The purpose of the experiments was to visualize deformation and break-up of oil droplets in the turbulent flow, and eventually localize flow regions responsible for the emulsification process. In parallel experimental campaign the flow of the same water/oil emulsions was investigated at the Uni-

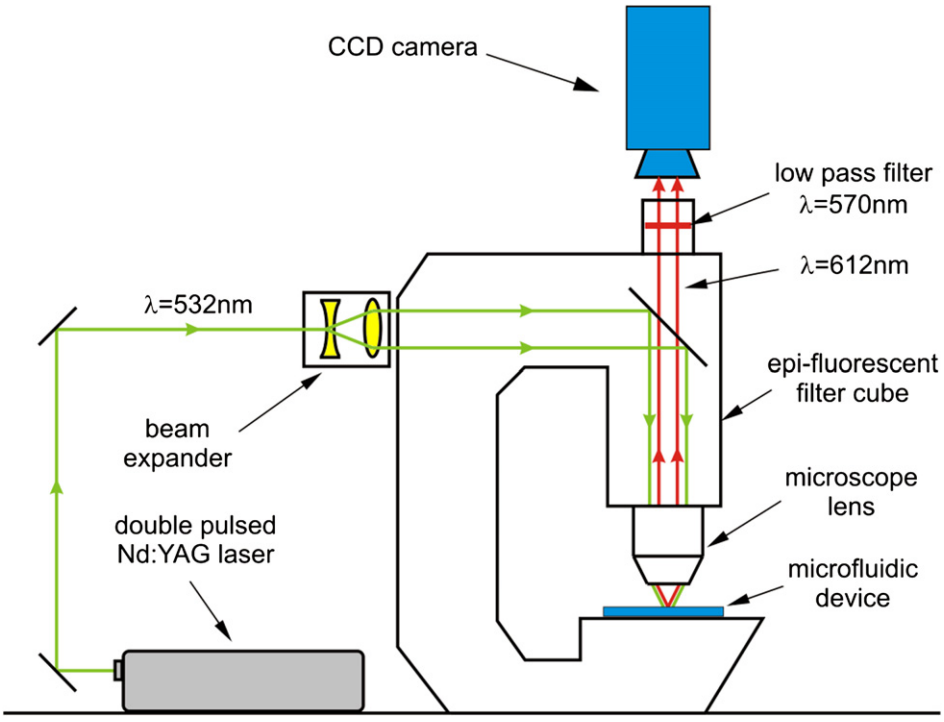

Fig. 3. Scheme of the micro-PIV experimental set-up with the epi-fluorescence microscope, CCD camera, and Nd:YAG laser.

versity of Sophia [1] using an exact replica of the emulsifier. There, detailed measurements of the droplets size distribution were performed, and results of the experiment are used in the comparisons given in the following.

The flow was examined using epi-fluorescence microscope (Nikon Eclipse 50i). To obtain different magnification ratios four far field lenses were used: 4x (NA 0.13/WD 17.1 mm), 10x (NA 0.3/WD 17.30 mm), 20x (NA 0.35/WD 24 mm), and 50x (NA 0.45/WD 17 mm). The flow observed under the microscope is characterized by large relative displacements; therefore application of high-speed recording techniques becomes essential. In our case, the image width of 1280 pixels corresponds, for the highest magnification ratio, to the object dimension of 0.172 mm. With flow velocity of 1 m s^{-1} the illumination time necessary to freeze the motion is below 100 ns. Such short illumination time can only be achieved by using pulsed laser light.

Three different light sources were tested: (i) built-in microscope halogen lamp with condenser for backlight illumination; (ii) CW 5W Argon laser (496 nm + 515 nm) for epi-fluorescence and flow visualization; (iii) Nd:YAG 30 mJ (532 nm) double pulsed laser used for epi-fluorescence flow velocity measurements (micro-PIV) and as a 5 ns short backlight illumination imaging droplets deformation.

For the flow study two high-resolution (1280×1024 pixels) 12 bit cameras were used. For the short exposure imaging the *PCO SensiCam* camera was used. When coupled with the double pulse laser it permits acquisition of two images at the minimum time interval of 200 ns and exposition time of 5 ns. However, with this system, pairs of images can be registered at about 3.75 Hz repetition rate only. Hence, the second camera *PCO1200hs* was used for high-speed flow visualisation. This camera permits recording of full resolution images (1280×1024 pixels) at 636 fps, and at over 40 kfps for decreased vertical image resolution. Although an electronic shutter of the camera allows to freeze relatively high-speed motion, it is attained at the cost of overall light intensity. With continuous illumination (halogen lamp, argon laser) the shortest feasible illumination time using this camera appeared to be 1 ms.

The flow structure measurements were performed for pure water seeded with fluorescent tracers. The micro-flow measurements based on epi-fluorescence illumination and high-speed imaging allowed for collecting detailed data on the shear stresses in the turbulent flow, necessary for modelling of the emulsification process. Thereafter, for the same flow conditions, the visualization of oil droplets in a very dilute emulsion was performed. As mentioned before, it is assumed that flow structure is not affected by the presence of droplets and results obtained for the single phase are applicable for calculation of the droplets deformation.

3. Flow structure measurements

The flow structure study was based on micro-PIV technique. It permits measurements of instantaneous two-dimensional velocity fields for the selected sections of the channel. The micro-PIV measurements were performed within the gap of the flat type emulsifier (Fig. 1). Distilled water was used as a working fluid. It was pumped under pressure through a small slit between the obstacle and side walls of the channel. Observations of the flow were performed through a transparent top wall. Flow was analysed in the vicinity of the channel centre defined by the vertical symmetry plane. The micro-PIV velocity measurements were performed using seeding of fluorescent polystyrene spheres, 2 μm in diameter (Duke Scientific Inc.). The particle

volumetric concentration was very low (<0.0001 %wt), hence they did not affect the flow structure. Particle Image Velocimetry (PIV) [12,13] based on correlation of pairs of images was used to evaluate instantaneous velocity fields in the channel. These full field data allowed evaluation of local velocity gradients, hence for estimation of conditions for the droplet breakup [14].

Unlike typical PIV methods, micro-PIV does not utilize a thin laser sheet to illuminate the seeding particles. The whole investigated volume was flooded with the laser light using beam expander and the microscope objective (Fig. 3) [15]. Once the particles are exposed to 532 nm light (green) from the laser, they emit red light with an emission maximum at 612 nm, as specified by the supplier.[1] The time-span in which particles continue to fluoresce after the laser pulse is of the order of nanoseconds, so motion induced blurring of the particles does not occur in the PIV images. Two low pass filters, mounted between the objective and the camera, permit only the fluorescent red light to pass, while preventing the green laser light to be detected by the camera. The micro-PIV images present well detectable bright spots of the seeding particles. Only particles being within the depth of focus are recorded. Particles that are out of focus add background noise, limiting applicability of the technique to thin layers of fluid (max. 10–15 mm). The flow was illuminated and observed through the upper window of the channel. By traversing the field of observation in the horizontal and vertical direction, the position of the interrogated flow plane was selected. The vertical resolution depends on the depth of field of the objective. For the micro-PIV experiments performed using the 10x objective the vertical resolution was estimated to be 10 μm and each PIV measurement covered area of about 0.7 mm × 0.55 mm. The horizontal resolution of the velocity field measurements for this objective was 0.5 μm. The accuracy of the velocity measurement depends on several experimental factors (quality of the images, seeding concentration, particle displacement), as well as on the vector evaluation procedure. Using in house developed software and by evaluating uniform, predefined flow of water through the micro-channel, the error of velocity measurement was estimated to be below 5%.

As results, five sets of velocity fields were obtained from the micro-PIV measurements—each of them in different locations within and behind the micro-channel (comp. Fig. 4 and Table 1). Measurements at positions P1 and P2 were obtained for the centre plane of the gap ($Y = -0.2$ mm), and used to evaluate velocity profiles along the x-direction in the vicinity of the gap entrance and the gap exit. Measurements at positions P3, P4 and P5 were performed for 20 planes, changing focal distance of the microscope from the vicinity of the upper glass wall down to the centre plane of the outlet channel (Table 1). It permitted us to evaluate development of the flow structure along the y-direction at three investigated locations, i.e. $x = 1$ mm, $x = 3$ mm and $x = 8$ mm behind the gap.

In order to quantify the turbulence in the channel, the ensemble-averaged velocity fields were calculated at each

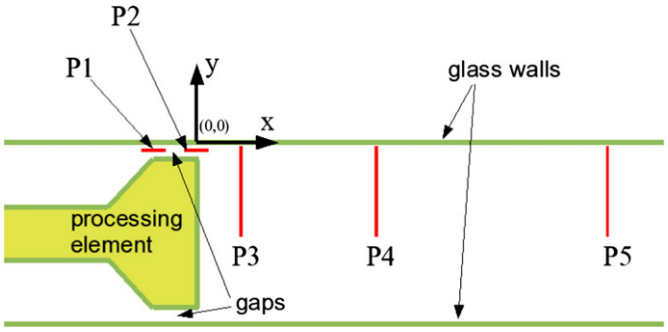

Fig. 4. Schematic drawing of the emulsifier with the coordinate system and locations of the measured velocity fields: P1–P5.

Table 1
Profiles span for selected locations

Profile location	X [mm]	Y [mm]
P1	from −1.45 to −0.7	−0.2
P2	from −0.35 to 0.35	−0.2
P3	1	from 0 to −3.75 in 0.1 ÷ 0.3 mm steps
P4	3	from 0 to −3.75 in 0.1 ÷ 0.3 mm steps
P5	8	from 0 to −3.75 in 0.1 ÷ 0.3 mm steps

analysed location. For the locations P1 and P2 (within the gap) the micro-PIV measurements were repeated up to hundred times. For the locations P3, P4 and P5 (behind the gap) measurements was repeated 28 times for each of 20 planes of selected channel depths. The frequency of the PIV measurements was 3.75 Hz, defined by the repetition rate of Nd:YAG laser. The time interval between measurements was long enough to obtain a set of independent measurements of the velocity field. Each measured velocity field consists of 1160×900 vectors. The assumption of homogeneity of the velocity field within the small area covered by our micro-PIV measurements was used to evaluate mean values. The velocity was averaged over the velocity field and than over all 28 measurements taken at the interrogated location P3–P5 (over 100 measurements at P1 and P2). Hence, the ensemble-averaged velocity profiles obtained at the locations P3, P4 and P5 are obtained by averaging set of about 10^7 vectors.

Velocity measurements performed at two positions P1 and P2 within the gap indicate that the flow through the gap fields is practically steady, no temporal flow field fluctuations could be observed for these two locations. For the position P1 the streamwise velocity of the flow rapidly increases from 8 to 16 m s^{-1} (Fig. 5) in the vicinity of the entrance to the gap, but it remains steady in time. Despite high velocities flow seems to be laminar, as can been seen in Fig. 5(a). Velocity measurements for the location P2 show flow development in the vicinity of the gap exit. Just behind the gap streamwise flow velocity rapidly decreases from 18 to 16 m s^{-1} (Fig. 6). Some initial spatial flow perturbation become visible here (Fig. 6(a)), indicating beginning of the transition to turbulence.

The main reason of the observed flow acceleration and deceleration is the rapid change of the channel height in the vicinity of the processing element. The channel height converges from 1.5 mm before the gap to 0.4 mm in the gap, and expands to

[1] For interpretation of the references to colour to this and other figures see online version of this article.

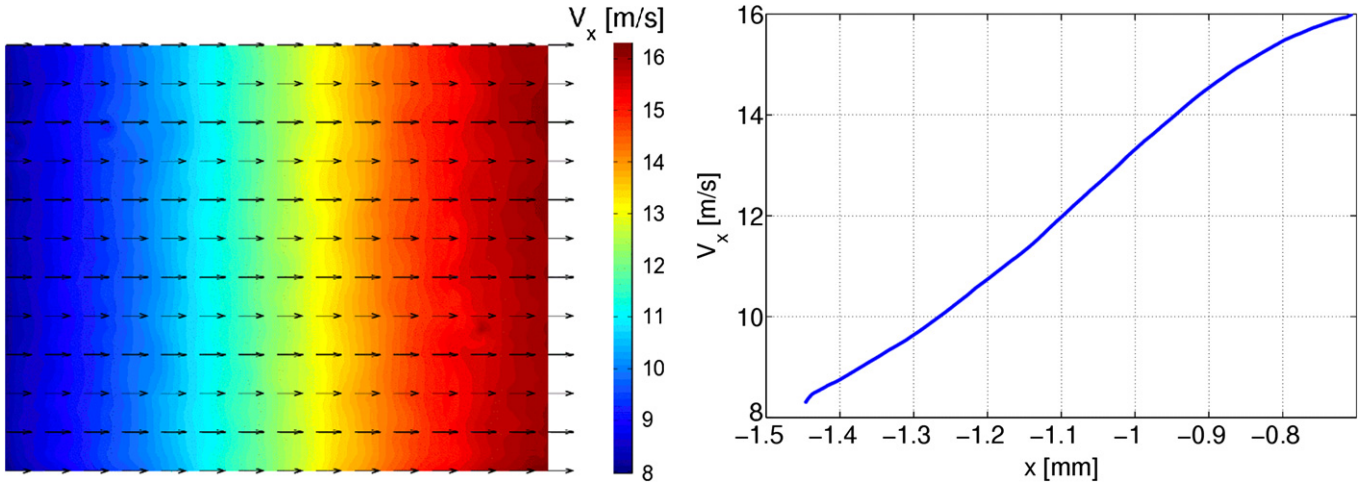

(a) (b)

Fig. 5. Location P1; (a) velocity vector field and velocity magnitude; image width corresponds to about 0.7 mm; (b) extracted profile for the x-component of velocity along the x-direction; position $x = -1$ corresponds to the entrance to the gap.

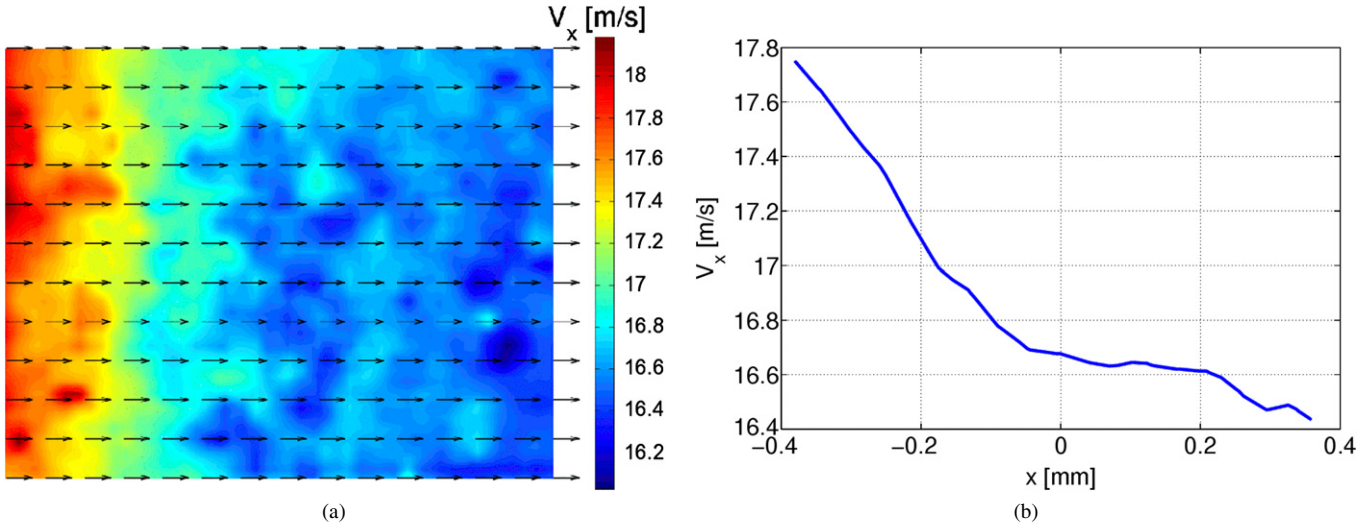

(a) (b)

Fig. 6. Location P2; (a) velocity vector field and velocity magnitude; width of the image corresponds to about 0.7 mm; (b) extracted profile for the x-component of velocity along x-direction; position $x = 0$ corresponds to the gap exit.

7.5 mm behind the gap. Due to the fluid acceleration and deceleration strong shear stresses are produced in the flow. In case of flow of emulsion these regions of high energy dissipation can be responsible for the break-up of the oil droplets.

Shortly after the processing element the flow velocity apparently changes its character, both flow direction and velocity amplitude strongly vary in time (comp. Fig. 7).

Three-dimensional structure of the velocity field after the processing element was acquired by collecting PIV measurements performed for three different distances (P3, P4, P5 in Fig. 4) at 20 y-planes. Each micro-PIV measurement was repeated 28 times for the same location to calculate mean flow velocity and its fluctuation. These micro-PIV measurements were used to evaluate profiles of the time-averaged x-component of velocity along the y-direction, i.e. channel height. Figs. 8 collect averaged velocity profiles (blue solid lines) obtained for three analysed locations P3, P4 and P5. The coordinate value $y = 0$ corresponds to the surface of the upper glass wall (comp. Figs. 1 and 4), and value $y = -3.75$ mm corresponds to the centre of the emulsifier. Symbols $\langle V_x \rangle$ and $\langle V_z \rangle$ indicate the mean values of the velocity x-component V_x and z-component V_z, respectively. It is worth noting high velocity "jet flow" present in the vicinity of the top wall. The reversal flow can be found closer to the channel axis, indicated in the profiles as negative values of the flow velocity (comp. Fig. 8(c)). Flow recirculation region created behind the processing element can be responsible for trapping dispersed droplets and enhancing their coalescence.

For evaluating turbulent characteristics of the flow behind the processing element, the fluctuating velocity components V'_x and V'_z were calculated using standard relations:

$$V_x = \langle V_x \rangle + V'_x$$
$$V_z = \langle V_z \rangle + V'_z \quad (1)$$

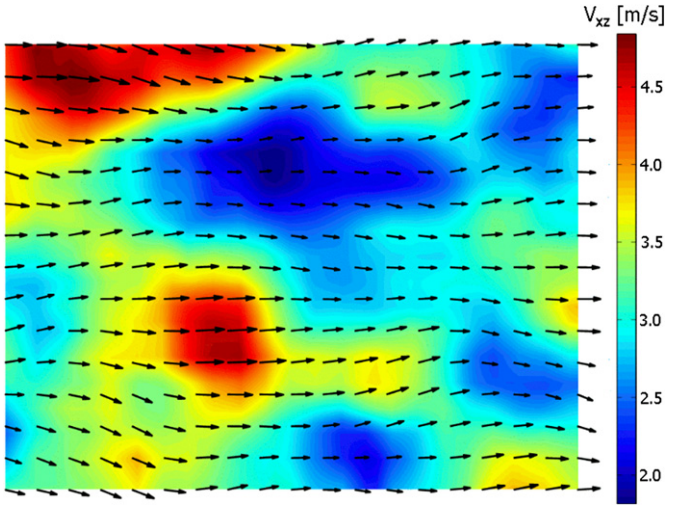

(a)

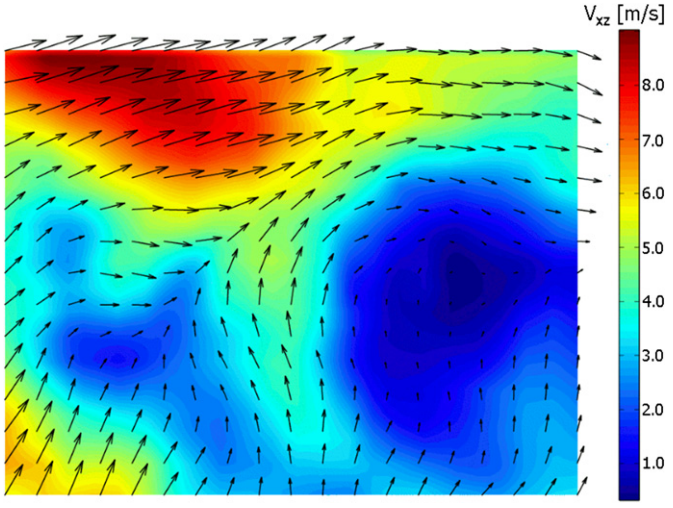

(b)

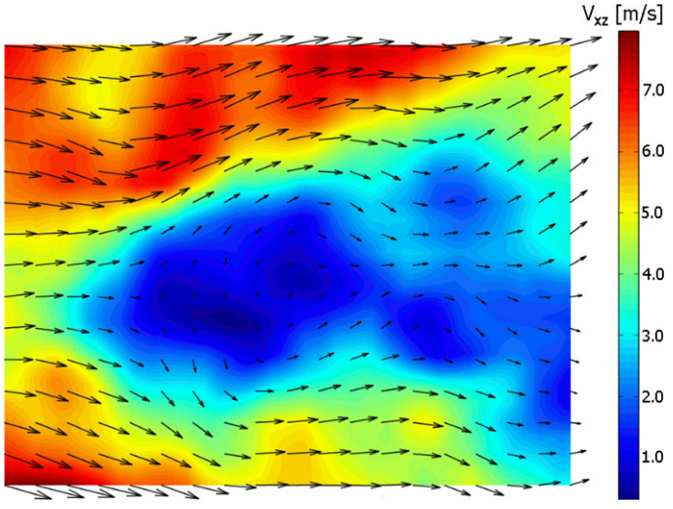

(c)

Fig. 7. Examples of the instantaneous velocity maps measured at the three different distances from the processing element: (a) $x = 1$ mm, (b) $x = 3$ mm, (c) $x = 8$ mm. Magnitude of vectors is coded by color. Width of image is about 0.7 mm in real space. The measurements were taken for $y = -0.3$ mm (0.3 mm bellow the top glass wall).

The total Turbulent Kinetic Energy *TKE* of the analysed flow field can be defined as:

$$TKE = 0.5\left(\left\langle V_x'^2\right\rangle + \left\langle V_y'^2\right\rangle + \left\langle V_z'^2\right\rangle\right) \tag{2}$$

For two-dimensional velocity measurements a modified turbulent kinetic energy (tke_{xz}) was defined, obtained from two available horizontal components of the velocity:

$$tke_{xz} = \left\langle V_x'^2\right\rangle + \left\langle V_z'^2\right\rangle \tag{3}$$

Figs. 8(a)–(c) show the variation of tke_{xz} (red dashed line) calculated for selected locations P3, P4 and P5. Profiles of turbulent kinetic energy tke_{xz} indicate that turbulent fluctuations emerge just behind the gap and persist along the x-direction. The tke_{xz} reaches its maximum about 0.3 mm below the glass wall. This is the region, where intense mixing occurs between high speed fluid arriving from the gap and low velocity recirculating flow behind the processing element. The peak value of the tke_{xz} is observed for the last interrogated position P5, i.e. about 8 mm from the gap.

In addition to providing mean velocity profiles, velocity fluctuations and turbulent kinetic energy, the micro-PIV data can also provide information on the large scale turbulent structures in the flow. One statistical quantity that can be used to describe the persistence of the turbulent structures is the second order structure function. It can be used to examine transition of viscous and inertial range of the turbulent flow [16]. The second order transverse structure function is defined as a mean square increment of the velocity component perpendicular to the line of separation l. For the velocity components V_x and V_z it is defined as:

$$\begin{aligned} S_X^{\perp}(l) &= \left\langle \left[V_X(x, z+l) - V_X(x, z)\right]^2 \right\rangle \\ S_Z^{\perp}(l) &= \left\langle \left[V_Z(x+l, z) - V_Z(x, z)\right]^2 \right\rangle \end{aligned} \tag{4}$$

The second order longitudinal structure function is defined as a mean square increment of the velocity component in the direction of two points separation. For the velocity components V_x and V_z and point separation l it is defined as:

$$\begin{aligned} S_X^{\parallel}(l) &= \left\langle \left[V_X(x+l, z) - V_X(x, z)\right]^2 \right\rangle \\ S_Z^{\parallel}(l) &= \left\langle \left[V_Z(x, z+l) - V_Z(x, z)\right]^2 \right\rangle \end{aligned} \tag{5}$$

The assumption of homogeneity of velocity field within the small area covered by our PIV measurements was used in these calculations. Mean square increments were averaged for certain separation l over whole velocity field obtained from the micro-PIV measurements. Then, the curves showing dependence of the structure function on the separation distance l were calculated. Finally, several curves, obtained from different PIV measurements made for the same flow, for the same location, and for the same level y were averaged. The longitudinal and transverse second order structure functions were evaluated from measured velocity fields at the three interrogated locations P3, P4 and P5, behind the processing element. The results for V_x velocity component for locations P3 and P5 are displayed in Figs. 9 and 10.

Fig. 9(a) shows transverse structure functions of V_x velocity component, obtained for location P3, i.e. 1 mm behind the

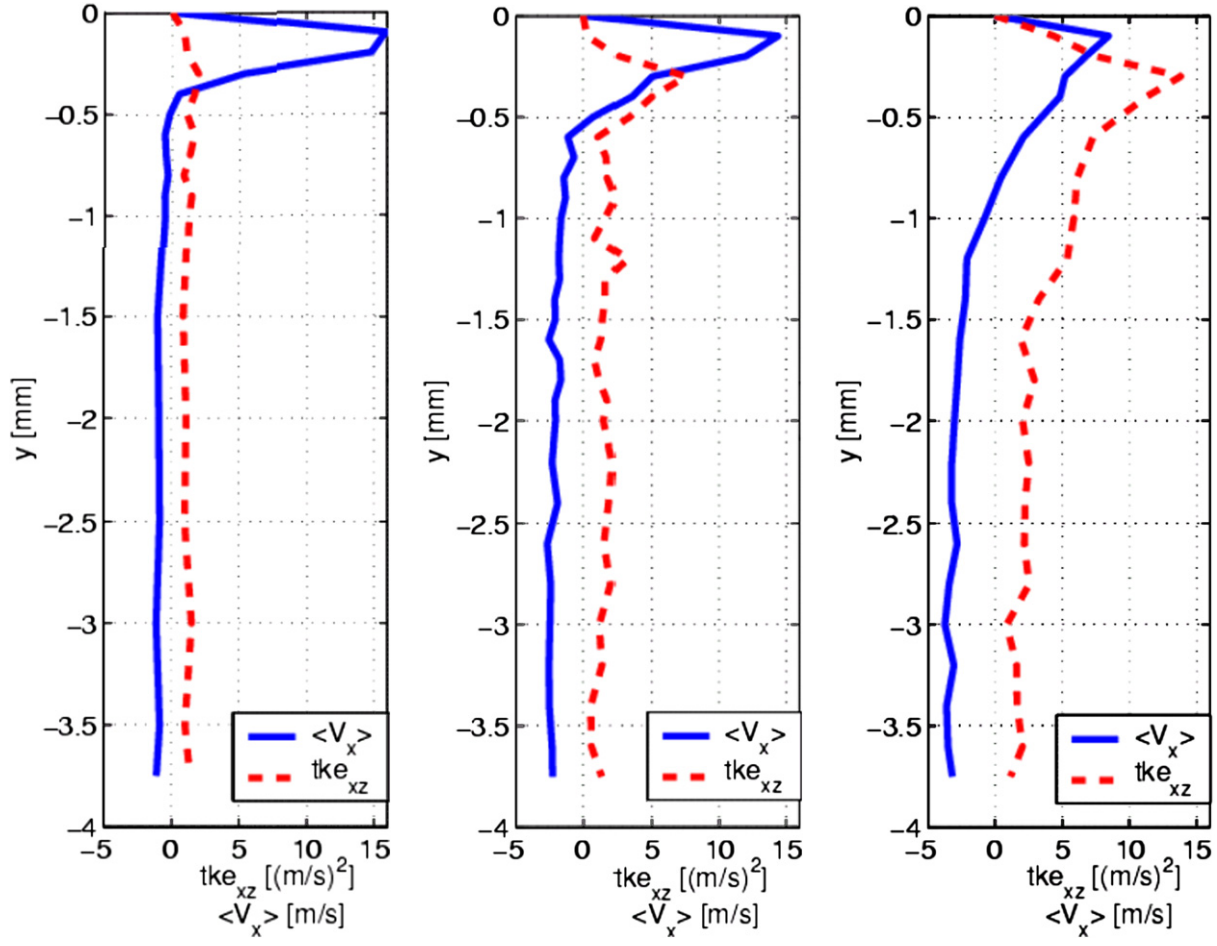

Fig. 8. The time-averaged x-component of velocity $\langle V_x \rangle$ (blue solid line) and turbulent kinetic energy tke_{xz} (red dashed line) obtained along y-direction for locations: (a) P3, (b) P4 and (c) P5.

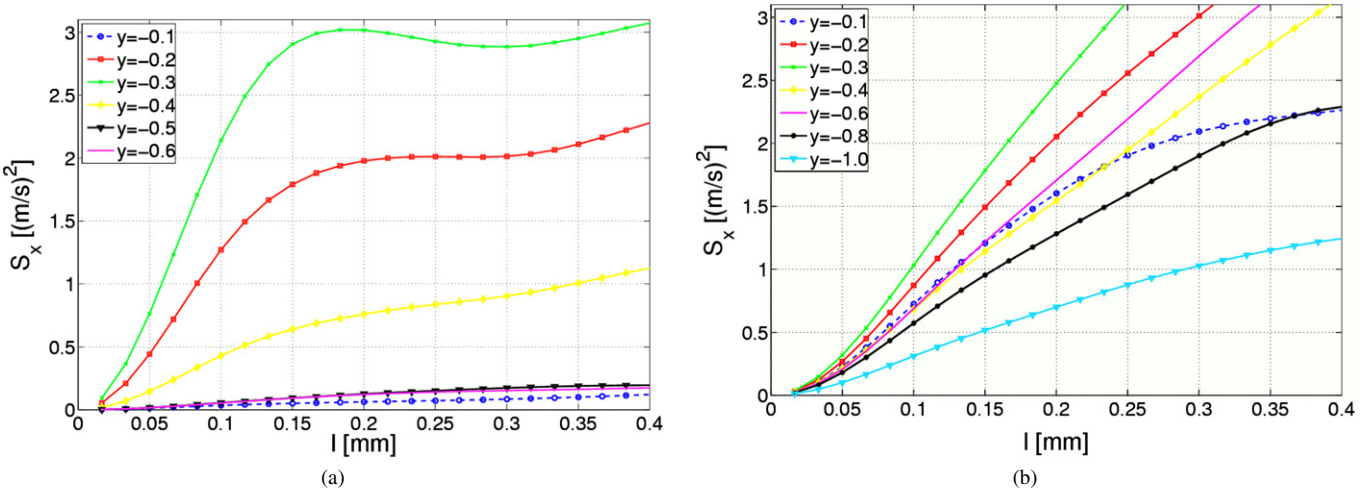

Fig. 9. The second order transverse structure functions for x-component of velocity V_X evaluated for different channel depths y at two locations: (a) P3 (1 mm behind gap) and (b) P5 (8 mm behind gap).

gap. Fast initial rising of the transverse structure function is observed for the channel depths $y = -0.2$ mm (red line) and $y = -0.3$ mm (green line). However, both curves flatten for larger separation length, starting already from $l > 0.15$ mm. Transverse fluctuations of velocity can be used to identify development of turbulent vortices. Hence, it can be deduced that near the end of the gap small but strong vortices are dominant structures of the velocity field. Distribution of the transverse structure function for this location exhibits increased values mainly for the levels $y = -0.3$ mm, $y = -0.2$ mm and $y = -0.4$ mm.

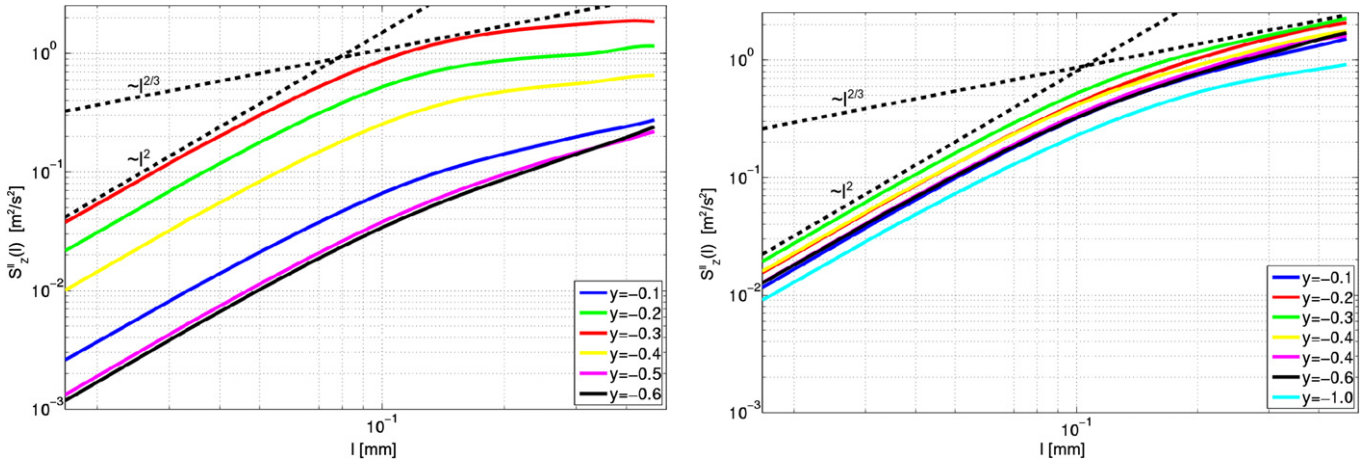

(a) (b)

Fig. 10. The second order longitudinal structure functions for x-component of the velocity V_X displayed in log–log scale for different channel depths y at two locations: (a) P3 (1 mm behind gap); (b) P5 (8 mm behind gap). Straight lines indicate initial slope exponent (l^2) and asymptotic slope exponent ($l^{2/3}$).

It indicates that, for location P3, the region of high velocity increments develops between $y = -0.1$ mm and $y = -0.5$ mm, with the maximum value at $y = -0.3$ mm (0.3 mm below the glass window). For the location P5 (8 mm behind the gap) the maximum of velocity increments remains at the channel depth $y = -0.3$ mm (green line in Fig. 9(b)), but high velocity gradient is also relatively large at other depths. It can be deduced that there is a trail of high velocity gradients, which is thin near the end of the gap and expands along the x direction.

Fig. 10 collects evaluated longitudinal structure functions for two positions: 1 mm and 8 mm from the gap. In the logarithmic scale one may find $2/3$ exponent for the asymptotic slope of the structure functions at higher separations l. Close to the gap the $2/3$ slope is mainly visible for structure function obtained for the depth -0.3 mm (Fig. 10(a)). Farther on (Fig. 10(b)) all profiles almost merge together following $2/3$ slope. Despite relatively small Reynolds number of the analysed flow, turbulent flow structure seems to follow Kolmogorov theory in this region.

4. Visualization of droplets break-up

Nearly the same flow system was used to analyse emulsification process for the dilute oil-water emulsion. For visualization of droplets deformation and break-up the modified emulsifier with a transparent processing element was used. It permitted backlight illumination of the flow in the gap between the processing element and the top glass window. The illumination is necessary for identifying oil droplets passing through the gap. Short laser light pulses were used to freeze under the microscope images of fast moving droplets. However, an object illuminated with a coherent light from the laser exhibits a speckled appearance (comp. Fig. 11). It seriously diminished contrast and resolution of recorded images of droplet.

Emulsions were prepared using 10 mM NaCl solution in de-ionised water as a continuous phase. Two continuous phase systems were tested, one without surfactant and one with 1 %wt anionic surfactant sodium dodecyl sulphate (SDS). Two silicone oils were used as a dispersed phase: S50 ($\mu = 0.05$ Pa s) and S500 ($\mu = 0.5$ Pa s). All experiments were done for the same flow rate $Q_V = 0.204$ dm^3 s^{-1}. The same emulsion was used in the parallel experimental campaign performed at the University of Sophia. In their experiment [1,4] the drop size distribution was measured for the emulsion created after over 100 consecutive passes through the emulsifier. A small samples of emulsion were extracted from the collecting vessel and investigated under the microscope equipped with the CCD camera and VCR recorder. The steady state droplet size measurements were performed after the experimental run. Hence, only stable, fine emulsion was present in the analysed sample.

In the present experiment dynamic imaging of droplets transported by the high speed flow was performed. The flow observation was done using *Nikon Eclipse 50i* epi-fluorescent microscope equipped with 20x lens and *PCO SensiCam* camera. Double pulse *Nd:YAG* laser (532 nm, 30 mJ per pulse) was used as a light source. The laser light pulse duration of 5 ns ensured to freeze images of fast moving droplets. Two consecutive images of emulsion were taken at the interval of 1 μs and used to evaluate instantaneous velocity magnitude of the individual droplet. Measured velocity of small droplets (below 15 μm) matched, within experimental uncertainty, the local fluid velocity obtained from the micro-PIV measurements. It confirms assumption that the flow structure remains unchanged for the dilute emulsion.

Over one thousand of flow images were taken and analysed. Figs. 11 illustrate recorded deformation and break-up of large droplets observed behind the gap. The image width corresponds to 432 μm. The elongated droplet observed in Fig. 11(a) formed nearly 0.5 mm long liquid thread before it eventually broke-up. A few small, hardly visible droplets of emulsion are also present in the viewing area of the images shown in Figs. 11. Their diameter is of the order of 10 μm and corresponds to the average droplet size measured by Tcholakova et al. at the University of Sophia [1].

Visualisation of droplets break-up in the emulsifier indicated that the emulsification process takes place just a few millime-

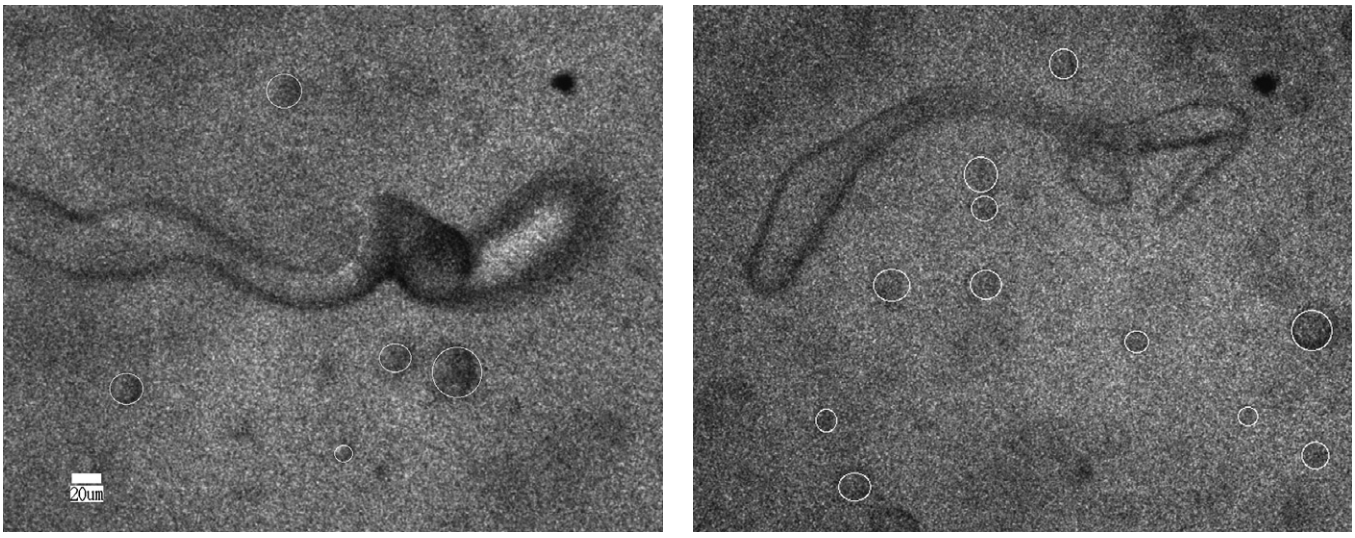

(a) (b)

Fig. 11. Images of deformed oil droplets recorded using 5 ns Nd:Yag laser flashes. Observation performed behind processing element and 0.4 mm below glass wall for the S50 silicone oil emulsion: (a) without surfactant and (b) with 1 %wt SDS surfactant; image width corresponds to 432 μm. Hardly visible small droplets are marked with circles. The 20 μm scale is shown as the reference dimension.

tres behind the processing element. Besides fine droplets typical for the final emulsion, also "large" droplets, like those visible in Figs. 11, were found behind the gap. Surprisingly, in the whole sequence of images we could not find evidence of "large" droplets break-up process within the gap. Only droplets in the size range of 10 μm could be found there. The presence of the "large" droplets behind the gap (Fig. 11(a)), and their absence in the gap is confusing. It is not obvious how the large droplets are created behind the gap. Maybe it is due to the agglomeration of small droplets in the dead-water region created by the recirculation zone behind the gap. It is also possible that some large droplets were trapped by the side walls of the gap and could not be observed by the camera. These droplets may have entered the re-circulation zone and, being transported by a cross-flow to the flow axis, could appear in the observation area. It would indicate the existence of a strong cross-flow in this region. In fact, high velocity fluctuations were found behind the gap by the velocity measurements described above.

5. Numerical simulation

Numerical simulations of the flow of water were done using CFD code *Fluent* (Fluent Inc) [17] to elucidate mechanisms responsible for the droplet break-up. Two types of numerical simulations were performed. To evaluate flow fluctuations direct unsteady simulation (DNS) was performed by solving the Navier-Stokes equations without any turbulence model. In the separate computational runs the averaged Navier-Stokes equations were solved using $k-\varepsilon$ turbulence model. These computations delivered the averaged flow structure and the turbulent dissipation rate in the vicinity of the processing element.

The DNS model allows to obtain accurate, unsteady solution of unmodified Navier–Stokes equations by resolving the whole range of spatial and temporal scales of the turbulence, from the smallest dissipative scales (Kolmogorov scales), up to the integral scale, associated with the motions containing most of the kinetic energy. The numerical domain used in the simulations had to cover full 3D geometry of the physical channel. All the spatial scales of the turbulence must be resolved in the computational mesh. Hence, very fine mesh and small time steps were used. The direct numerical simulation (DNS) performed with the classical finite volume code implemented in Fluent is time consuming and vulnerable. Nevertheless, it appeared that for the investigated geometry it was possible to obtain reasonable solutions reproducing typical for the turbulence flow characteristics. These results were compared with the outcome of the steady, average turbulence model, where the flow symmetry was assumed and only one quarter of the model geometry was used for the computational domain.

The turbulent flow model assumes a priori that the flow is turbulent and properly described by the averaged variables using Reynolds hypothesis. The reliability of the simulation results depends on several empirical parameters, assumed to be applicable to the specific flow configuration. The main advantage of using the average turbulence models is their computational efficiency. The computations were performed using standard $k-\varepsilon$ model with default parameters and an enhanced wall treatment. The average model permits to assume flow symmetry, therefore only one-quarter of the physical domain was implemented into the computational scheme, extremely improving computational efficiency.

Fig. 12 displays schematic of the computational domain. The total axial extension of the computational domain was 177 mm, including 97.5 mm inlet length, 1 mm gap length, and 78.5 mm outlet length. The channel width and height are those corresponding to the physical model (comp. Fig. 2). In both computational models structural hexahedron mesh with boundary layer was generated in the gap and in the vicinity of the processing element. The tetrahedron mesh was used in the remaining

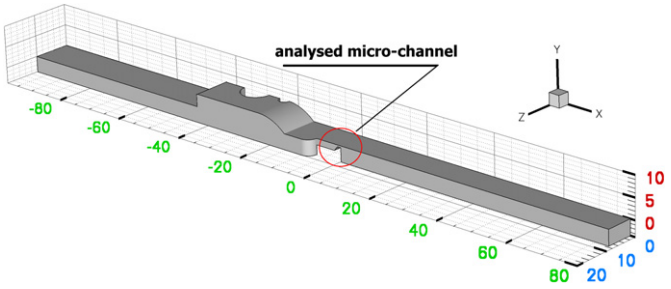

Fig. 12. Schematic of geometry of the computational domain used for the numerical simulations. The origin of the coordinate system is at the gap exit ($x = 0$) and the top wall ($y = 0$). One quarter of the emulsifier is shown with 97.5 mm long inlet, 1 mm long gap, and 78.5 mm outlet.

Table 2
Parameters of the unsteady laminar flow model (Direct Numerical Simulation)

Used package and version	Fluent 6.2.16, double precision, segregated
Flow type	three-dimensional, laminar, unsteady, incompressible
Medium	water, constant density $\rho = 998.2\ \mathrm{kg\,m^{-3}}$ and viscosity $\mu = 0.001003\ \mathrm{Pa\,s}$
Mass flow-rate	$Q_M = 0.204\ \mathrm{kg\,s^{-1}}$
Inlet	mass-flow inlet
Outlet	pressure outlet
Discretization scheme	Pressure: standard Momentum: Second Order Upwind
Time step size	10^{-7} s
Geometry and grid	whole model geometry, 1 745 830 cells of the grid

parts of the computational domain, reproducing all geometrical details of the emulsifier.

Several mesh resolution tests were performed to evaluate the grid convergence index (GCI) [18], and to identify the optimal mesh resolution, being compromise of the computational time and the numerical accuracy. The most critical flow region is within the gap. The optimal mesh sought using convergence grid index and applying mesh adaptation technique for the gap region was found for the turbulent model to consist of nearly 0.5 mln grid cells. For the DNS model it was found that sufficient accuracy was obtained for the gap mesh of $50 \times 30 \times 50$ nodes, and the total number of computational cells for the whole domain amounting over 1.7×10^6. Direct numerical simulation allows for an unbiased analysis of turbulent flow, to extract physical fluctuations and to perform user

Table 3
Parameters of the steady turbulent flow model

Used package and version	Fluent 6.2.16, double precision, segregated
Flow type	three-dimensional, steady, incompressible
Viscosity model	standard $k-\varepsilon$ turbulence model with Enhanced Wall Treatment
Medium	water, constant density $\rho = 998.2\ \mathrm{kg\,m^{-3}}$ and viscosity $\mu = 0.001003\ \mathrm{Pa\,s}$
Mass flow-rate	$Q_M = 0.051\ \mathrm{kg\,s^{-1}}$ (one quarter of $Q_M = 0.204\ \mathrm{kg\,s^{-1}}$)
Inlet	mass-flow inlet turbulence intensity 12.1% hydraulic diameter 0.0109
Outlet	pressure outlet turbulence intensity 12.1% hydraulic diameter 0.0109
Discretization scheme	Pressure: standard Momentum: Second Order Upwind Turbulence Kinetic Energy: Second Order Upwind Turbulence Dissipation Rate: Second Order Upwind
Geometry and grid	one quarter of the model geometry, 457 473 cells of the grid
Grid adaptation	dynamic adaptation based on velocity magnitude gradient: refine threshold 0.0001, interval: 20 iterations $Y+$: allowed value 1–2

defined averaging of the flow. The optimal time step of the simulation was estimated by performing several computational tests. It was found to be equal 0.1 μs. The averaged flow characteristics were well reproduced using about 200 time steps, i.e. by averaging turbulent fluctuations over 0.2 ms time interval. Detailed parameters of the computational models used for the direct numerical simulation and for steady turbulent flow model are collected in Tables 2 and 3, respectively.

Fig. 13 shows velocity field obtained from DNS flow simulation averaged over 180 time steps. It can be found that before the gap the average flow velocity is about 5 $\mathrm{m\,s^{-1}}$. In the gap strong acceleration of the flow occurs and velocity peak values reach about 23 $\mathrm{m\,s^{-1}}$. Velocity time series extracted for several cross-sections of the channel indicated that turbulent fluctuations at the inlet of the gap are very low, about 1% only. The fluctuations amplitude quickly increases along the channel to reach at its exit high frequency modulation with nearly 8% amplitude. Fig. 14 shows turbulence intensity obtained from DNS

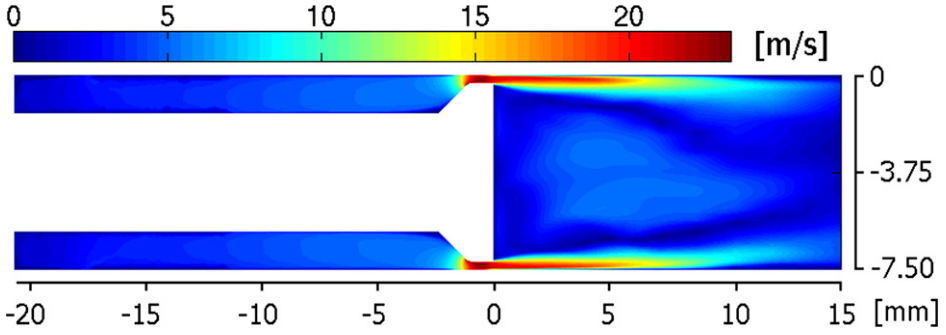

Fig. 13. Contour map of the time averaged velocity field obtained for the central cross-section of the emulsifier central part for the DNS model.

simulations at five distances along the channel. It is evaluated for 180 instantaneous flow fields according to the formula:

$$I = \frac{|V_X - \langle V_X \rangle|}{\langle V_X \rangle} \cdot 100\% \tag{6}$$

Numerical simulation permits to evaluate all three components of the velocity fluctuations, however to compare obtained results with the experimental data two-dimensional projection of the flow field was used. Mean square value of the velocity fluctuations V'_X and V'_Z were obtained from the direct numerical simulation, and the turbulent kinetic energy tke_{XZ} was evaluated as previously in the experimental part (3).

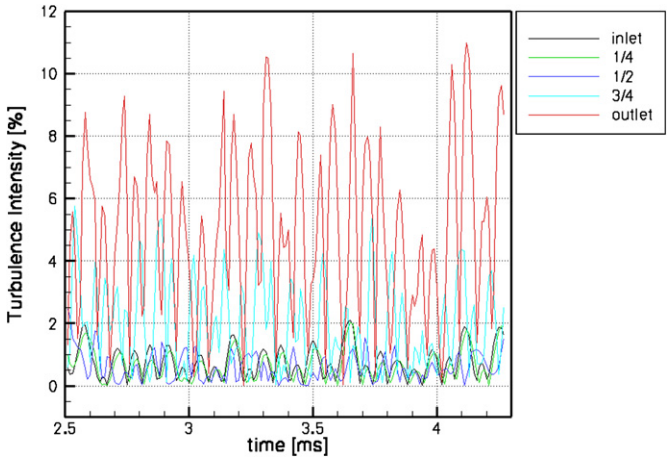

Fig. 14. Development of the turbulence intensity in the gap. Velocity fluctuations evaluated from DNS simulations for longitudinal velocity component V_X at five locations along the micro-channel: inlet ($x = -1$ mm), 1/4 ($x = -0.75$ mm), 1/2 ($x = -0.5$ mm), 3/4 ($x = -0.25$ mm), and outlet ($x = 0$).

Comparison performed for the two representations of turbulent kinetic energy obtained through numerical simulations revealed very small differences between distribution of the tke_{XZ} and the total value of *TKE*, justifying use of the two-dimensional *TKE* representation, imposed by our experimental constrains. Fig. 15 shows that flow turbulence, i.e. the averaged velocity fluctuations reached their maximum about 6 mm behind the gap, in relatively good agreement with the experimental data obtained from the PIV measurements.

Direct numerical simulations utilize large amount of the computer resources and computational time. Analysis performed using averaged turbulent model, applied to one-quarter of the cavity, confirms main futures of the flow field obtained by direct numerical simulation. Figs. 16 shows the average velocity vector field for the longitudinal section along central part of the model in the vicinity of the gap and in the region behind processing element. Velocity magnitude attains maximum value of about 20 m s^{-1} in the gap between processing element and the top wall. It can be found that recirculation flow behind the gap region is quite significant. Velocity magnitude of the reverse flow is about -2 m s^{-1} (blue vectors in Fig. 16).

Comparison of the numerical and experimental results was done to validate the numerical simulations. Fig. 17 combines profiles of the x-component of the velocity, obtained from the numerical simulations using turbulent model (green line), averaged field from the direct numerical simulation (red line), and averaged micro-PIV measurements (blue line). They are compared at three locations behind the processing element: 1 mm (Fig. 17(a)), 3 mm (Fig. 17(b)), and 8 mm (Fig. 17(c)). Qualitative and quantitative agreement of the numerical and experimental results in the vicinity of the processing element is fairly good (Figs. 17(a), (b)). For the profile located 8 mm behind the processing element (Fig. 17(c)) the difference between nu-

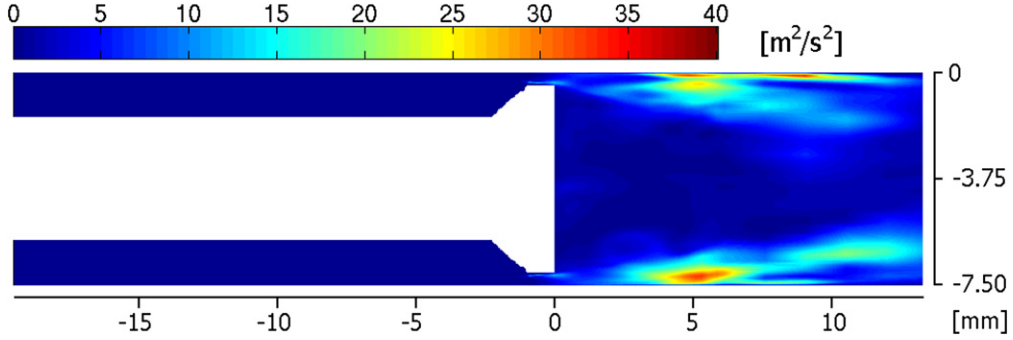

Fig. 15. Direct numerical simulation, contour map of mean square value of the velocity fluctuations obtained for the central cross-section of the emulsifier.

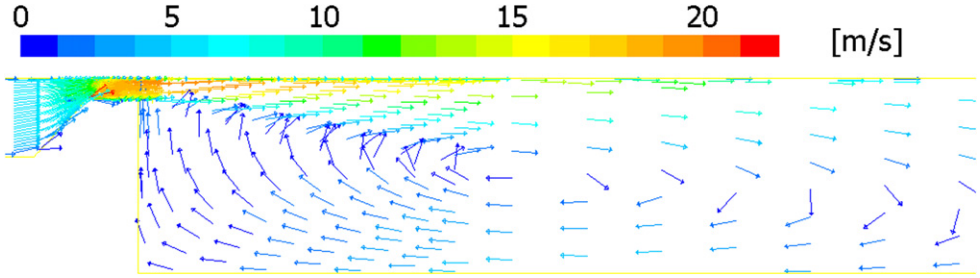

Fig. 16. Velocity vector field in the vicinity of the processing element, turbulent numerical model.

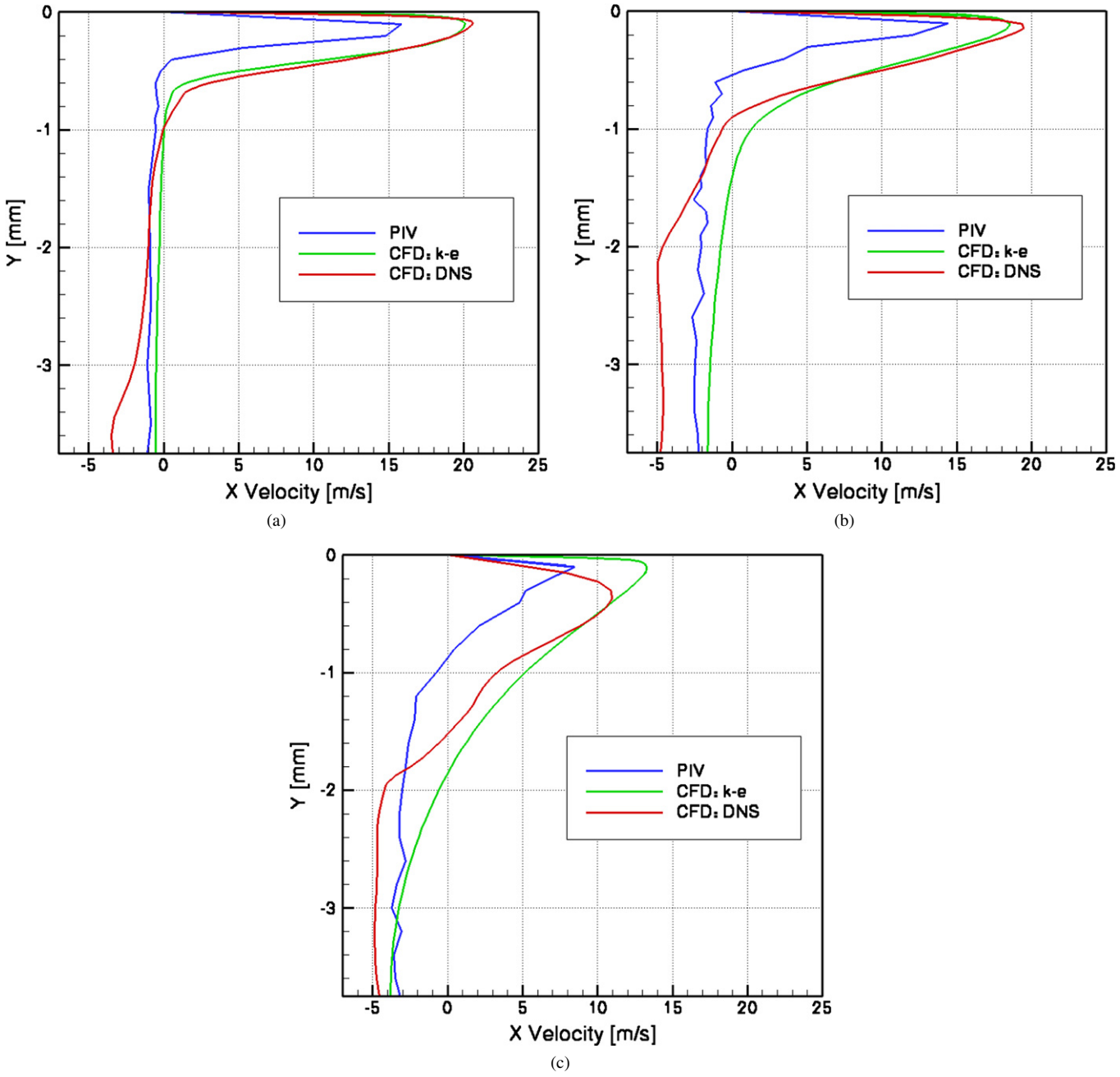

Fig. 17. Comparison of the numerical and experimental longitudinal velocity profiles evaluated along the channel depth for the three locations behind the processing element: (a) 1 mm; (b) 3 mm; (c) 8 mm. PIV—experimental data obtained form micro-PIV; CFD $k-e$—turbulent numerical model; CFD-DNS—direct numerical model.

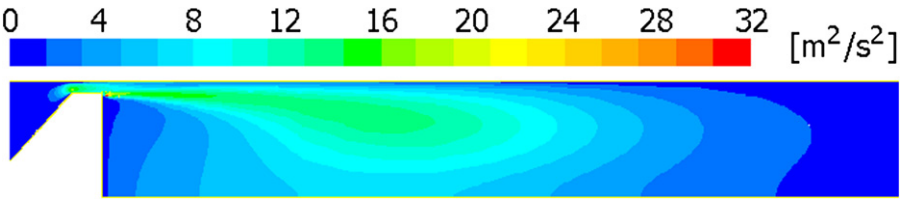

Fig. 18. Contours of the turbulent kinetic energy along the gap evaluated using $k-e$ numerical model.

merical and experimental results becomes significant, although location of the velocity maximum is relatively well preserved. Presence of the strong reverse flow behind the gap is probably responsible for diminishing of the resolution of the PIV evaluation, which in turn decreases peak magnitude of the measured velocity vectors.

Evaluation of velocity gradients as well as instantaneous velocity field fluctuations may permit to identify flow regions responsible for the droplets break-up. In the laminar flow regime one expects that size of the droplets is determined by the balance between the characteristic flow shearing forces acting on the droplet and interfacial tension. Maximum shear rates are present inside the gap, reaching the peak value of $10^6\ s^{-1}$ at inner wall of the gap entry. The shear rate computed in course of DNS simulations was used in the following part to estimate theoretical size of droplets produced by shear-induced break-up process.

In the turbulent flow droplets break-up rate is related to the magnitude of the kinetic energy dissipation. Distribution of the turbulent kinetic energy, obtained from the numerical simulations (Fig. 18) shows that maximum value of turbulent kinetic energy is reached in the region just behind the processing element. It is where the intense mixing of the high velocity fluid ejected from the gap with the low velocity recirculating flow behind the processing element takes place. Similar result is obtained from direct numerical simulation. However, turbulent model indicates maximum of turbulent energy dissipation rate at the gap entry, where both direct numerical simulation and micro-PIV experiment indicate very little amplitude of velocity fluctuations.

Fig. 19 shows profile of the averaged turbulent energy dissipation rate ε evaluated along the gap from the turbulent numerical model. It is visible that ε has a sharp maximum just at the inlet of the gap. The maximum value of turbulent energy dissipation rate is about $\varepsilon^{\max} = 1.160 \times 10^6\ m^2\,s^{-3}$. At the end of the gap turbulent dissipation rate rapidly decreases to the value of about $\varepsilon = 1.9 \times 10^5\ m^2\,s^{-3}$. The averaged value over the whole gap is $\varepsilon^{\text{avg}} = 3.599 \times 10^5\ m^2\,s^{-3}$. These numbers are comparable with those obtained by Steiner et al. [4] for the turbulent flow in the axially-symmetric emulsifier. The question arises, which value of ε is responsible for the final size of the emulsion droplets? It can be argued that peak values of the turbulent dissipation rate should be relevant for the resulting droplets distribution. However, relaxation time of large droplets can be too long to allow for their strong deformation during only 0.5 μs time of passage through the micro-channel formed by the gap. Their passage through the tiny region where the energy dissipation rate has its maximum (comp. Fig. 19) takes even much less time. For comparison the averaged and maximum values of ε were used to test credibility of two widely used models of the droplet break-up in turbulent flow field.

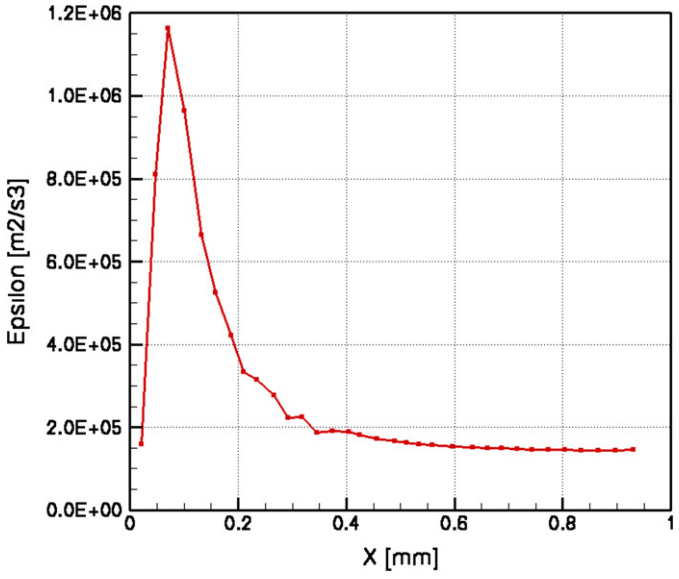

Fig. 19. Horizontal profile of the averaged turbulent dissipation rate ε through the gap evaluated using $k-\varepsilon$ numerical model.

6. Estimation of the droplets size

One of the simplest configurations to describe and observe droplet break-up is analysis of single droplet in a shear flow. This topic stems from classical experiments of G.I. Taylor [19] that were motivated by an interest in emulsion formation. According to simple derivations, it was shown that in case of small viscosity ratio between droplet and carrier, the droplet interface deformation in the shear flow can be described as a relatively regular transformation of a sphere to an ellipsoidal form. Under critical deformation ratio the droplet breaks into two satellite droplets. The condition for such break-up depends on the surface tension, shear rate and viscosity of fluids only. A simple relation below allows for evaluation of the equilibrium droplets radius d at such flow conditions:

$$d = \frac{\sigma(\mu_d + \mu)}{G\mu(\frac{19}{4}\mu_d + 4\mu)} \tag{7}$$

where: μ—dispersing medium viscosity, μ_d—dispersed medium viscosity (drops viscosity), σ—interfacial tension, G—velocity gradient.

The ratio $\mu G d/\sigma$ is usually called Capillary number and for viscosity ratio μ_d/μ close to one gives simple estimation of the droplet break-up conditions. In the investigated geometry regions of highest velocity gradients correspond to high velocity regions in the gap. The estimate for maximum G delivered by the direct numerical simulation is about $G_{\text{avg}} = 1.6762 \times 10^5\ s^{-1}$. This value was used to calculate expected droplets for less viscous oil, i.e. for viscosity ratio equal 50. It results with the droplet diameter equal 6.9 μm.

Experimental verification of the Taylor formula is known to give reasonable agreement only for laminar flow and for systems of viscosity ratio close to one. Therefore, the above estimate has rather little practical value for the investigated case. For the fully developed turbulent flow energy transferred from the smallest scale eddies, defined as the turbulent dissipation energy, is responsible for droplet break-up. Using the turbulent dissipation energy estimated from the numerical model the expected oil drop size was evaluated. Two different models of droplet break-up in turbulent flow field were tested. In the first model formulated by Hinze [20] viscous effects on droplet break-up process are neglected, and the following estimate of the droplet diameter is given:

$$d_{\max} = 0.749\frac{\sigma^{3/5}}{\rho^{3/5} \cdot \varepsilon^{2/5}} \tag{8}$$

Table 4
Results of the oil drops diameter estimation using turbulent energy dissipation rate ε from the numerical simulations

	Hinze model both oils [μm]	Davis model oil S50 [μm]	Davis model oil S500 [μm]
Max. epsilon value in gap $\varepsilon_{max} = 1.160 \times 10^6\ m^2\,s^{-3}$	1.97	6.46	32.77
Avg. epsilon value in gap $\varepsilon_{avg} = 3.599 \times 10^5\ m^2\,s^{-3}$	3.14	8.95	44.01

Experimental data for the mean droplet diameter are 10.1 μm for S50 oil and 20.7 μm for S500 oil [1].

where: d_{max}—maximum oil droplet diameter, σ—interfacial tension, ρ—dispersing medium density, ε—turbulent energy dissipation rate.

The second analysed model was proposed by Davis [21]. The model incorporates effect of the viscosity of the dispersed phase. Here, the droplet diameter is given by:

$$d_{max} = \frac{K}{\rho^{3/5} \cdot \varepsilon^{2/5}} \left(\sigma + \frac{\mu_d \sqrt{2} (\varepsilon \cdot d_{max})^{1/3}}{4} \right)^{3/5} \quad (9)$$

where: d_{max}—maximum oil droplet diameter, K—constant ($K = 0.748$), σ—interfacial tension, ρ—dispersing medium density, ε—turbulent dissipation rate, μ_d—dispersed phase viscosity.

The droplet size estimation was done for two silicone oils used in the experiments with emulsions: oil S50 with viscosity 50 mPa s, and oil S500 with ten times higher viscosity. Hence, the viscosity ratio was 50 and 500, respectively. The continuous phase used in the analysed here emulsification experiment [1,4] was de-ionised water with 1 %wt anionic surfactant sodium dodecyl sulphate (SDS). The density and surface tension used in the evaluations were $\rho = 998\ kg\,m^{-3}$ and $\sigma = 5.5\ mN\,m^{-1}$, respectively. Table 4 collects results of estimation of the oil droplets diameter obtained by applying the two turbulent droplet break-up models described above. Calculation was done for two silicone oils and for two estimates of the turbulent dissipation rate obtained in the numerical simulations: its maximum value in the gap ε_{max} and the averaged value over the whole gap ε_{avg}.

Precise experiments performed at the University of Sophia [1] for the model of emulsifier indicate droplets mean diameter to be 10.1 and 20.7 μm for silicone oils S50 and S500, respectively. The accuracy of the optical droplet size measurements was estimated to be ±0.3 μm [22]. Obviously, the droplets size predicted by the Hinze model (Table 4) severely overestimates the effects of turbulence on emulsification process, even for the smaller viscosity ratio (oil S50). The model seems to be not applicable for the investigated oil emulsions.

The droplet size prediction given by the Davis model appears to be more reliable, as it includes effects of the viscosity ratio. However, only the experimental data for less viscous oil (S50) are close enough to the model estimates, and only if the averaged value of the turbulent dissipation rate ε is used (comp. Table 4). It is worth noting that the simple estimate (7) made using the Taylor model [19] gives droplet size of 6.9 μm, surprisingly close to the estimate obtained using the Davis model.

For higher viscosity ratio (oil S500) the Davis model totally overestimates effect of increased viscosity of the dispersed media. The predicted droplet size differs by factor two from the experimental value. Probably it is due to the different break-up mechanism present in the case of very viscous droplets, where building of a long, cylindrical liquid threads dominates before their tip is disintegrated by the flow shear stress [14].

7. Conclusions

Velocity measurements (micro-PIV) indicated almost uniform velocity flow field in the short micro-channel formed by the gap region of the emulsifier. It means that turbulence is still not fully developed there, and only strong shear gradients could be responsible for the droplet break-up within the gap. Strong recirculation zone with the reversal of flow is found behind the processing element. The turbulent fluctuations of the velocity field and break-up of the flow symmetry, observed in this region, indicate that probably transition from laminar to turbulent flow regime occurs there.

Numerical modelling confirmed main details of the velocity flow field measured by the micro-PIV method. It gave us confidence that generated numerical data can be applied for predicting conditions for the droplets break-up in a shear flow. The DNS and turbulent flow models were successfully applied producing similar flow structure. It was found that intensity of turbulence is relatively low and that the droplets break-up process may depend not only on the turbulent dissipation energy but also on the shear gradients of the strongly fluctuating in time quasi-laminar flow field.

Acknowledgements

This investigation was conducted in the framework of EMMA project, supported by Austrian Ministry of Science and Education, contract no.: GZ 45.534/1-VI/6a/2003 CONEX. The micro-PIV expertise was developed in the framework of EU Thematic Network PIVNET2.

References

[1] G. Brenn (project coordinator), Emulsions with nanoparticles for new materials, Scientific report of EMMA Project, Graz University of Technology, Graz, 2005.
[2] K.D. Danov, P.A. Kralchevsky, K.P. Ananthapadmanabhan, A. Lips, Particle–interface interaction across a nonpolar medium in relation to the production of particle-stabilized emulsions, Langmuir 22 (2006) 106–115.
[3] P. Garstecki, Formation of bubbles and droplets in microfluidic systems, Bull. Pol. Ac.: Tech. 53 (2005) 361–372.
[4] H. Steiner, R. Teppner, G. Brenn, N. Vankova, S. Tcholakova, N. Denkov, Numerical simulation and experimental study of emulsification in a narrow-gap homogenizer, Chem. Engrg. Sci. 61 (2006) 5841–5855.
[5] E. Wajnryb, J.S. Dahler, The Newtonian viscosity of moderately dense suspension, Adv. Chem. Phys. 102 (1997) 193–313.
[6] S. Elghobashi, G.C. Trusdell, Direct simulation of particle dispersion in decaying isotropic turbulence, J. Fluid Mech. 242 (1992) 655–700.
[7] L.I. Zaichik, V.M. Alipchenkov, A.R. Avetissian, Modelling turbulent collision rates of inertial particles, Int. J. Heat Fluid Flow 27 (2006) 937–944.

[8] R. Sadr, M. Yoda, Z. Zheng, A.T. Conlisk, An experimental study of electro-osmotic flow in rectangular microchannels, J. Fluid Mech. 506 (2004) 357–367.
[9] J.G. Santiago, S.T. Wereley, C.D. Meinhart, D.J. Beebe, R.J. Adrian, A micro particle image velocimetry system, Exp. Fluids 25 (1998) 316–319.
[10] C.D. Meinhart, S.T. Wereley, J.G. Santiago, PIV measurement of a microchannel flow, Exp. Fluids 27 (1999) 414–419.
[11] H. Li, G. Olsen, MicroPIV measurements of turbulent flow in square microchannels with hydraulic diameters from 200 μm to 640 μm, Int. J. Heat Fluid Flow 27 (2006) 123–134.
[12] M. Raffel, C. Willert, J. Kompenhans, Particle Image Velocimetry, A Practical Guide, Springer-Verlag, Berlin, 1998.
[13] G.M. Quenot, J. Pakleza, T.A. Kowalewski, Particle image velocimetry with optical flow, Exp. Fluids 25 (1998) 177–189.
[14] H.A. Stone, Dynamics of drop deformation and break-up in viscous fluids, Ann. Rev. Fluid Mech. 26 (1994) 65–120.
[15] S. Blonski, T.A. Kowalewski, Micro-flows investigation in production process of emulsions containing nanoparticles, CD-ROM Proceedings of Euromech Colloquium 472, Grenoble, 2005.
[16] U. Frisch, Turbulence, Cambridge Univ. Press, Cambridge, 1995.
[17] Fluent 6, User's Guide, Fluent Inc., Lebanon, NH, 2002.
[18] P.J. Roache, Verification and Validation in Computational Science and Engineering, Hermosa Publishers, Albuquerque, NM, 1998.
[19] G.I. Taylor, The formation of emulsion in definable field of flow, Proc. R. Soc. Lond. A 146 (1934) 501–505.
[20] J.O. Hinze, Fundamentals of the hydrodynamic mechanism of splitting in dispersion process, AIChE J. 1 (1955) 289–295.
[21] J.T. Davis, Drop size of emulsions related to turbulent energy dissipation rates, Chem. Engrg. Sci. 40 (1985) 839–842.
[22] S. Tcholakova, N.D. Denkov, T. Danner, Role of surfactant type and concentration for the mean drop size during emulsification in turbulent flow, Langmuir 20 (2004) 7444–7458.